Fusion Engineering and Design 204 (2024) 114520

Contents lists available at ScienceDirect

Fusion Engineering and Design

journal homepage: www.elsevier.com/locate/fusengdes

Development of a scintillator based fast-ion loss detector for the Wendelstein 7-X stellarator

A. Jansen van Vuuren [a,b,*], J. Garcia-Dominguez [c], J. Hidalgo-Salaverri [d,e], J. Segado-Fernandez [d,e], A. LeViness [c], J. Ayllon-Guerola [d,e], J. Rueda-Rueda [b,d], S.A. Lazerson [f], J. Galdon-Quiroga [b], M. Garcia-Munoz [b,d], N. Pablant [c], the Wendelstein 7-X Team [1]

[a] Ecole Polytechnique Fédérale de Lausanne (EPFL), Swiss Plasma Center (SPC), CH-1015, Lausanne, Switzerland
[b] Department of Atomic, Molecular and Nuclear Physics, University of Seville, Spain
[c] Princeton Plasma Physics Laboratory, Princeton, NJ, United States of America
[d] Centro Nacional de Aceleradores (U. Sevilla, CSIC, J. de Andalucia), Seville, Spain
[e] Department of Mechanical Engineering and Manufacturing, University of Seville, Spain
[f] Max–Planck Institute for Plasma Physics, 17489 Greifswald, Germany

ARTICLE INFO

Keywords:
Magnetic confinement fusion
Fast-ion loss detector
Fast ions
Wendelstein 7-X

ABSTRACT

A new scintillator based fast-ion loss detector (FILD) system has been designed for the Wendelstein 7-X (W7-X) stellarator. The mechanical design of the system is presented here along with engineering analyses of the system. This includes an assessment of the structural loads which also considers electromagnetic forces calculated for possible disruption scenarios as well as a mode frequency analysis of the system. Furthermore, an analysis of the thermal characteristics of the actively cooled probe head under prescribed steady state and transient heat loads is presented. Finally, the optical relay system is described and its properties used to forward model synthetic camera signals using the FILDSIM code and based on theoretical fast-ion losses incident on the probe head calculated using the ASCOT5 code.

1. Introduction

The Wendelstein 7-X stellarator (W7-X) aims to demonstrate good fast-ion confinement for this line of magnetic-confinement fusion devices. The device has been optimized from a designed level for good fast-ion confinement [1,2], which is expected to improve for increasing plasma pressures [3]. In order to assess the results of this optimization effort, diagnostics are required to evaluate the confinement of fast ions during experiments on W7-X. A scintillator based FILD system has been designed to assist with this goal.

The so-called sFILD diagnostic, being developed by the Princeton Plasma Physics Laboratory in collaboration with the Max–Planck Institute of Plasma Physics and the University of Seville, is based on the conceptual design presented in [4]. This new diagnostic will complement the existing Faraday cup (FC) type FILD detectors installed on W7-X [5,6], being positioned directly adjacent to the FC-FILD [6]. In contrast to FC-FILDs which measure the current induced by fast ions impinging on a conductive plate, the sFILD will measure the light emitted by fast ions impinging on a plate covered with scintillating material. Scintillator based FILDs provide significantly higher velocity-space resolution and signal-to-noise ratios (SNR) as compared to FC-FILDs [7]. Furthermore, these detectors are immune from electromagnetic pickup which FC-FILDs can be susceptible to [8], allowing to unambiguously infer magnetohydrodynamic (MHD) induced fast-ion losses.

The manufacturing of the sFILD system has commenced with plans for the diagnostic to be installed on W7-X during the OP2 campaign. Here, a detailed design and analyses of the mechanical aspects of the system and its performance is presented. The paper is structured as follows, first a description of the detector is presented in Section 2 followed by a detailed description and analyses of the structural loads in Section 3. Next, an analysis of the thermal performance of the actively cooled probe head is presented, followed by a description of the optical relay subsystem 5. Finally, in Section 6 the expected optical signal is calculated for the detector by means of forward modelling.

* Corresponding author at: Ecole Polytechnique Fédérale de Lausanne (EPFL), Swiss Plasma Center (SPC), CH-1015, Lausanne, Switzerland.
E-mail address: anton.jansenvanvuuren@epfl.ch (A. Jansen van Vuuren).
[1] See author list of T. Sunn Pedersen et al. Nucl. Fusion **62** 042022.

https://doi.org/10.1016/j.fusengdes.2024.114520
Received 13 October 2023; Received in revised form 20 May 2024; Accepted 21 May 2024
Available online 28 May 2024

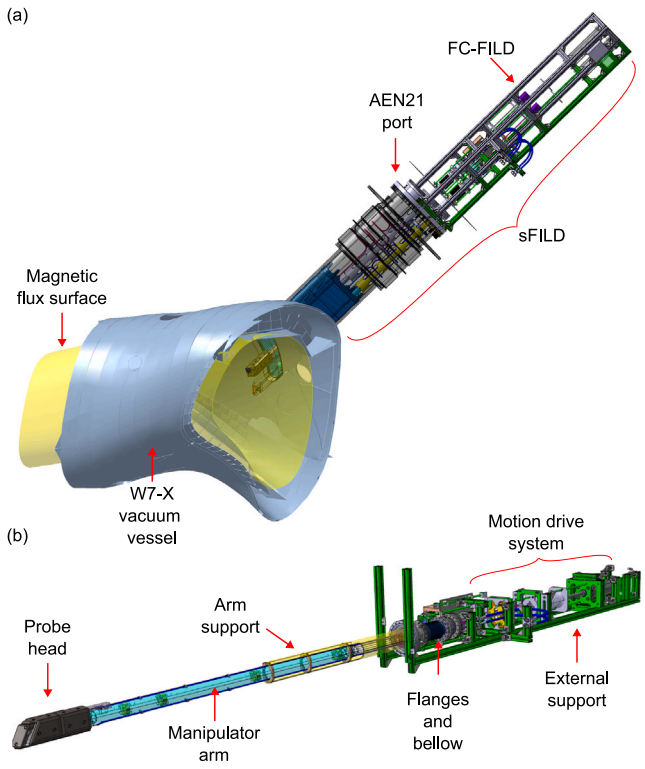

Fig. 1. (a) CAD illustration of the sFILD system attached to port AEN21 of the W7-X vacuum vessel. Here, only a relevant section of the vessel is shown as well as the shape of the last-closed magnetic flux surface (LCFS) near the diagnostic. (b) CAD drawing of the sFILD system with various subsystems indicated.

2. Design of a scintillator based FILD system for W7-X

Fig. 1a shows a CAD model of the sFILD diagnostic as planned to be installed on W7-X. The sFILD will attach to the lowermost of three sub flanges in the AEN21 port, with the centre flange supporting a separate Faraday cup based FILD system [6]. As can be seen in Fig. 1b, the diagnostic consists of a probe head which will house a scintillator plate positioned at the end of a manipulator arm. The manipulator arm will contain an optical system to relay light produced by fast ions entering the probe head through one of two slits and impacting on the scintillator plate to an ex-vessel mounted CMOS camera. Additionally, the manipulator arm will guide two stainless steel water cooling tubes, a single multimode fibre optic patch cable, a thermocouple cable and two co-axial cables between the probe head and feed through connections at the viewport flange. The fibre optic patch cable will be used to back-illuminate the scintillator plate to allow for calibration of the optical setup, while the co-axial cables will be used to transport the electrical signal generated by the detector plate doubling as a FC plate. The current extracted from the stainless steel plate covered by TG-Green scintillating material will provide a valuable additional measurement of the absolute flux of fast ions impinging on the detector plate. In contrast however to the existing FC-FILDs, this additional FC measurement will simply be an integrated measurement that will not provide information on the pitch and energy of incident ions. The manipulator arm will rest in cantilever on an inner stainless steel support structure shown in yellow with a 3 μm thick coating of Dynamant at the contact points for reduced friction.

A pneumatic motion drive system located on the ex-vessel section of the diagnostic will allow to plunge the manipulator and probe head up to 26 cm beyond the first wall elements, as shown in Fig. 2. The design of the motion drive system is based on that of the FC-FILD, but will

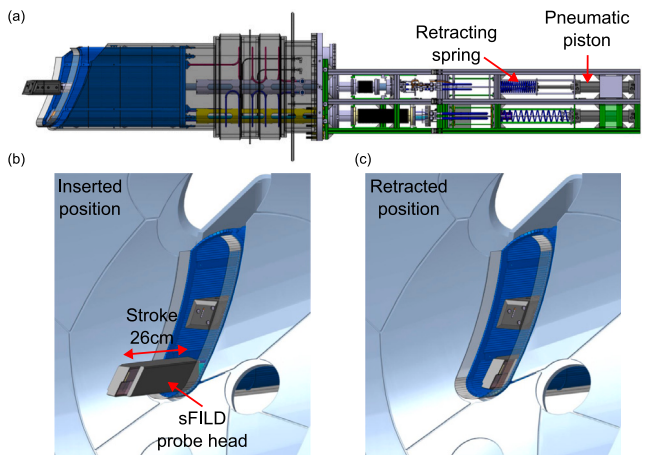

Fig. 2. (a) Side view of the FC-FILD and sFILD in the inserted and retracted positions, respectively. In-vessel views of the sFILD in the maximum (b) inserted and (c) retracted positions. The stroke of the sFILD is 26 cm.

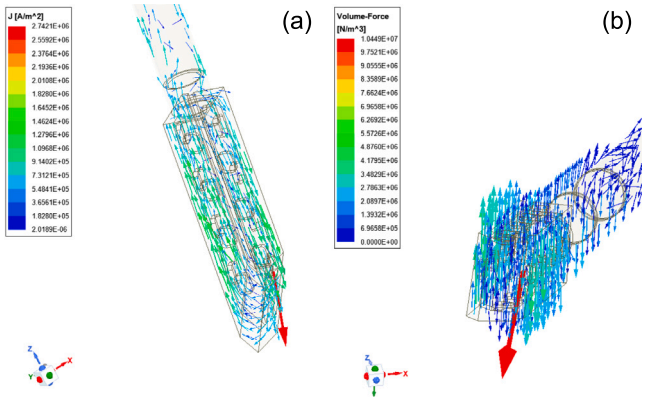

Fig. 3. Calculated (a) eddy currents generated in the sFILD probe head during a fast decay of the toroidal current simulating a disruption. (b) The associated **E**×**B** forces result in a 40 N m torsional load on the probe head.

operate independently. The pneumatic piston will be connected via a transmission rod to the in vessel manipulator arm. The exact insertion position will be controlled by a hard-stop set by an electrical motor. The insertion motion of the drive unit is countered by a spring which allows it to retract the probe head as needed.

3. Structural assessment

A detailed assessment of various mechanical loads on the sFILD and its subsystems has been performed using the ANSYS code. Firstly, we present an analysis of electromagnetic (EM) forces induced in the probe head during possible disruptions events performed using the Maxwell package of ANSYS. Two scenarios were investigated in this work, in the first scenario a loss of plasma toroidal current on a short timescale was considered. Conservatively, a maximum toroidal (bootstrap) current of 100 kA is considered to decay on a timescale of 1 ms. While in the second scenario a loss of plasma energy on the same time scale of 1 ms is considered. Conservatively, the assumption here is a plasma energy loss of 5 MJ corresponding to a total poloidal current of 1.6 MA.

A reduced CAD model of the sFILD in-vessel structure has been included in Maxwell, while the 3D magnetic field of W7-X is approximated by a purely toroidal magnetic field of 3.1 T. This is larger than the (nearly toroidal) field strength in the standard magnetic field configuration of 2.7 T in order to be conservative. Analysing the EM loads for the two scenarios discussed above found that only during the

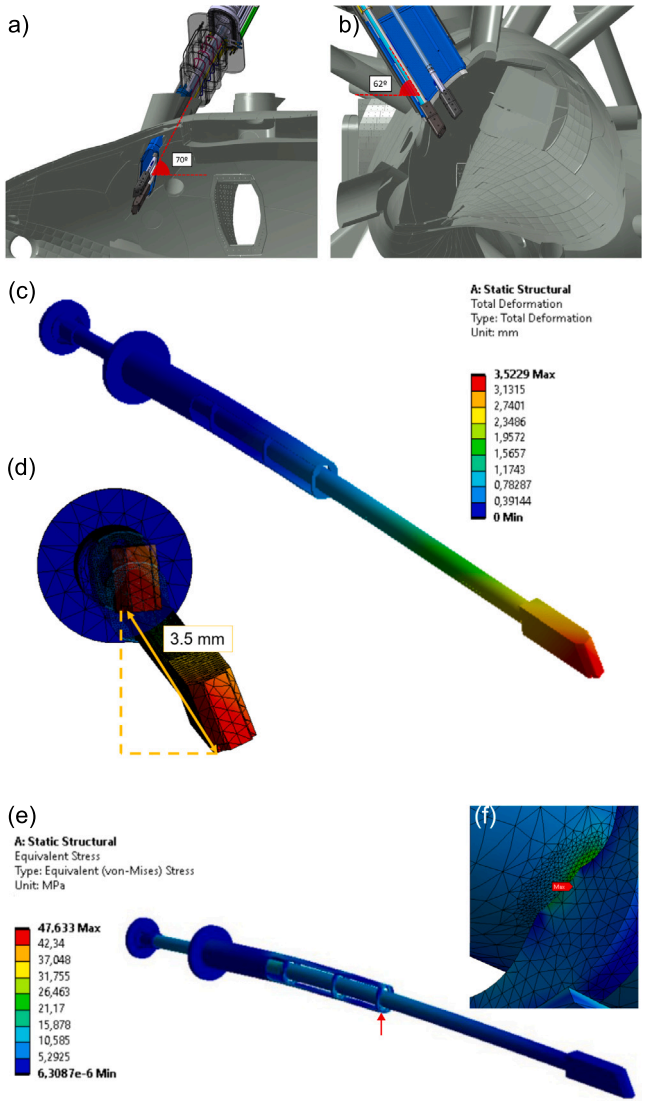

Fig. 4. (a) Frontal and (b) lateral in vessel views of the sFILD in W7-X. (c) Overview of the calculated deformation of the sFILD in mm. (d) Frontal view of the calculated deformation of the sFILD. The diagonal deformation (w.r.t the port orientation) occurs as a result of the tilt direction of the system. (e) General view of the equivalent Von Mises stresses in the sFILD diagnostic. (d) View of the equivalent Von Mises stresses at the contact between the first contact ring (red arrow) and the manipulator arm.

decay of the toroidal current a torsional load on the probe head of 40 N m is expected as shown in Fig. 3. Changes in the poloidal current is found to cause insignificantly small forces on the probe head.

These forces were included in the structural analysis of the sFILD manipulator arm under cantilever as can be seen in Fig. 4a and b. Here again, a reduced model of the sFILD was included in the ANSYS code to analyse through the use of the finite elements method the expected deformation and stress due to applied forces. The expected deformation of the manipulator system under cantilever is around 3.5 mm as shown in Fig. 4c and d. This represents a 0.15% deformation w.r.t the length of the system under cantilever. Importantly, this relatively small amount of deformation means no collision of the system with the narrow port structure is observed.

The maximum expected stresses are observed to occur at the contact between the manipulator guiding ring at the plasma facing end of the manipulator support structure, and at a cut-out corner of the support structure itself as seen in Fig. 4d and e. The magnitude of these stresses at both locations are around 48 MPa, well below the yield strength of the planned SS316LN stainless steel at 208 MPa.

Additionally, a mode and vibrational analysis was performed both for vibrations from the electrical grid at 50 Hz and with uniform frequencies to conservatively estimate response to seismic vibrations or vibrations from unexpected sources. The deformations and stresses from the grid frequency is negligible, and with a uniform vibrations with 1 g acceleration only small deformations (less than 4 mm) and stresses (less than 28 MPa) are calculated resulting in no collision with the port structure.

4. Thermomechanical assessment

Since the sFILD probe head will be a plasma-facing component it is expected to receive significant heat loads. Therefore, it is a W7-X requirement that the sFILD be actively cooled. In this section an analysis of the effectiveness of the active cooling is considered under prescribed heat loads as well as the incurred stress in the graphite tiles. The heat loads considered in the analysis include loads from stray microwaves from the electron cyclotron resonance heating (ECRH) system and black-body radiation due to the high temperature plasma in close proximity to the probe head. The stray ECRH contribution is considered to account for $200\,\mathrm{kW\,m^{-2}}$ in W7-X. However, as the steel probe head of the sFILD will be covered in graphite tiles with an absorption coefficient of 0.1 for the ECRH waves [9], the absorbed heat flux absorbed is estimated to be $20\,\mathrm{kW\,m^{-2}}$. The heat flux on the probe head due to the direct exposure to the high-temperature plasma is considered to be $100\,\mathrm{kW\,m^{-2}}$ as considered in [10]. Thus the combined stationary load is expected to be $120\,\mathrm{kW\,m^{-2}}$. Additionally, a transitory heat load from fast-ion losses from the neutral beam injection (NBI) heating sources is also considered. The NBI sources on W7-X can be used for up to 20 s and can produce up to $100\,\mathrm{kW\,m^{-2}}$ on the plasma facing components.

The ANSYS software package has again been used to assess the temperature and thermally-induced stress evolution over the probe head under the two scenarios. The geometry used includes the stainless steel probe head together with its graphite protection tiles. Each material has its own temperature-dependent properties. Fig. 5a shows a CAD model of the probe head, this model was slightly simplified for this assessment to the model presented in Fig. 5c and d to reduce computational time. Cooling channels (shown in Fig. 5b) with water at 25 °C at $3.5\,\mathrm{m\,s^{-1}}$ [10] will be used to cool the probe head. The convection coefficient in the inner walls of the cooling channels have been used to model the effect of the cooling water. For a channel diameter of 4 mm, the water convection coefficient has been estimated at $17\,000\,\mathrm{W\,m^{-2}\,K^{-1}}$ using the Dittus–Boelter correlation. As shown in 5c the stationary ECRH and radiation heat load has been applied uniformly on the front surfaces of the detector as they are the regions with a direct line of view with the plasma. The transient NBI associated heat load has been extended to the lateral faces closest to the plasma as a conservative approach as seen in 5d.

Results from the steady state, shown in Fig. 6a, show that the system can withstand the prescribed heat flux while staying well below the material limits. The maximum temperature that the graphite tiles reach in this scenario is 775 °C, while the graphite sublimation temperature is 2000 °C as found by [11]. Fig. 6b shows the temperature distribution over the probe head at the end of the NBI phase. As with the steady state scenario the wings of the graphite front tile are the hottest region, here the temperature reaches 985 °C, still well below the sublimation limit. Fig. 6c shows the temperature evolution of the maximum temperature over the probe head as the NBIs are considered. After the cooling period, the temperature goes below 800 °C. Considering that the sFILD will only measure during the NBI periods -when there are fast-ion losses- and that the NBI system has a dwell period of 6 min, it is safe to say that the probe head will have returned to its parking temperature after this time.

It should be noted that the heat loads considered in the thermal analysis are considered to be conservative. Operational experience from

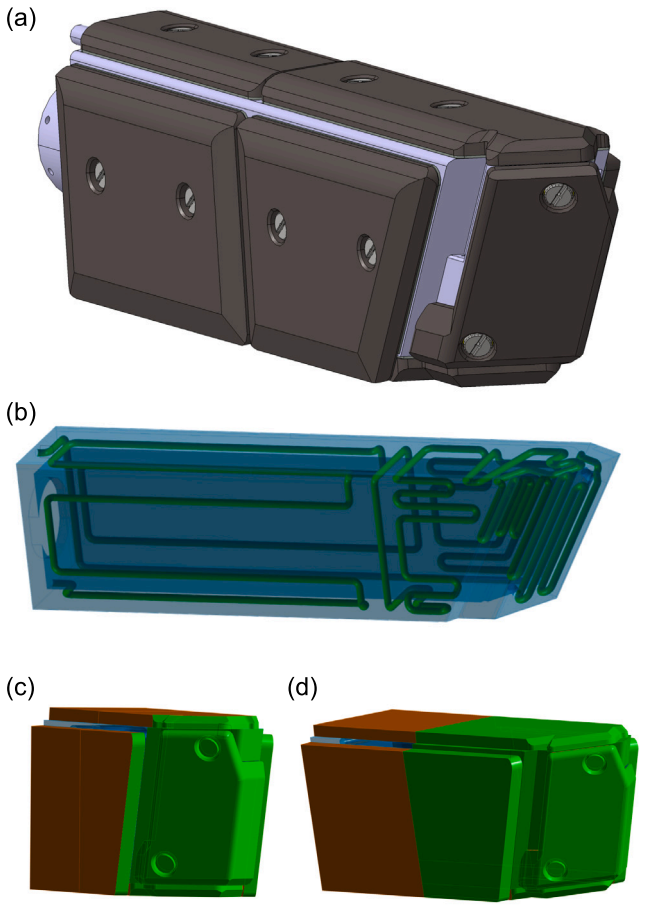

Fig. 5. (a) CAD model of the stainless steel probe head covered with graphite protection tiles. (b) View of the interior cooling channels of the probe head included in the ANSYS model. Surfaces (in green) where the heat fluxes were applied for the (c) ECRH and radiation, and (d) NBI losses.

the FC-FILD [6], which has been operating since the start of the OP2 campaign and is situated next to the planned sFILD position, has found that the FC-FILD probe head does not typically exceed temperatures of 100 °C during operation, with a maximum temperature of 180 °C degrees measured in a single discharge. Nonetheless, it is planned that the temperature of the sFILD probe head will be monitored using a thermocouple in contact with the probe head surface behind the scintillator plate. If the temperature exceeds a set safety value during operation, the probe will be retracted to its parking position, where plasma radiation loads will be reduced and, as shown in Fig. 6c, the probe should recover from transient heat loads in about 100 s. If the NBI operations are extended in the future to operation times longer than 20 s, and NBI-related heat loads are found to cause excessive heating at longer times, the probe could be inserted for phases with NBI only, reducing the contribution from stationary heat loads and allowing the probe head to cool to a safe value before being re-inserted for further measurements.

The maximum principal stress distribution is shown in Fig. 7a. Here, the regions affected by the bolt are marked with dashed red circles to show that these regions are out of the scope of this model and they are studied in a separate model. The tensile stresses up to 13 MPa are withing the allowed limit of 15 MPa which is half the material limit of 30 MPa for graphite. The minimum principal stress, Fig. 7b, distribution shows that the maximum compression is found on the connection between the short wing and the rest of the graphite tile. This corner reaches a compression of 45 MPa below the allowed limit of 85 MPa as graphite can withstand up to 170 MPa.

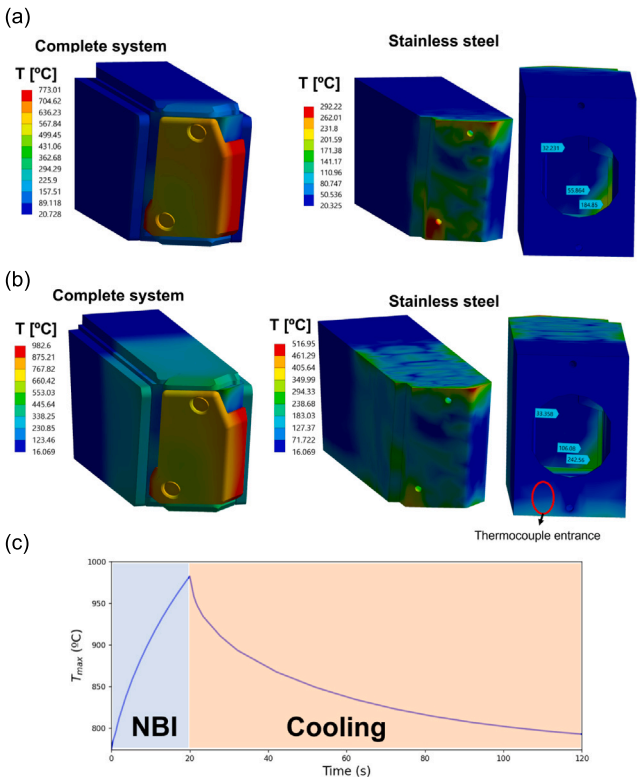

Fig. 6. (a) Steady state temperature distribution over the complete system and over the stainless steel block. (b) Temperature distribution after the NBI phase over the complete system and over the stainless steel block. (c) Evolution of the maximum temperature over the probe head.

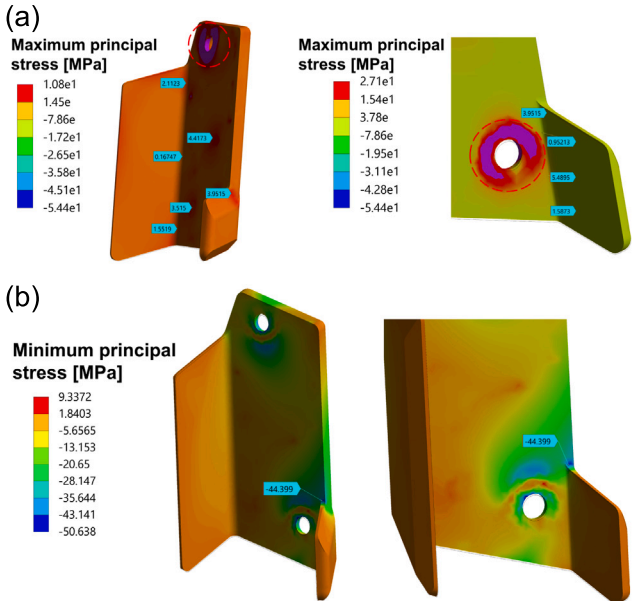

Fig. 7. (a) Maximum and (b) minimum principal stress distribution over the graphite front tile. Positive values are tensile and negative, compressive. The bolt attachment section circled in dashed-red is treated in a separate model.

The graphite protection tiles will be bolted to the sFILD stainless steel probe head using conical inconel washers (from Schnorr) as shown in Fig. 8a. Sigraflex strips will be placed between the tile steel to allow good contact between the surfaces, while the washer will be pretensioned to ensure contact is maintained between the tiles and steel

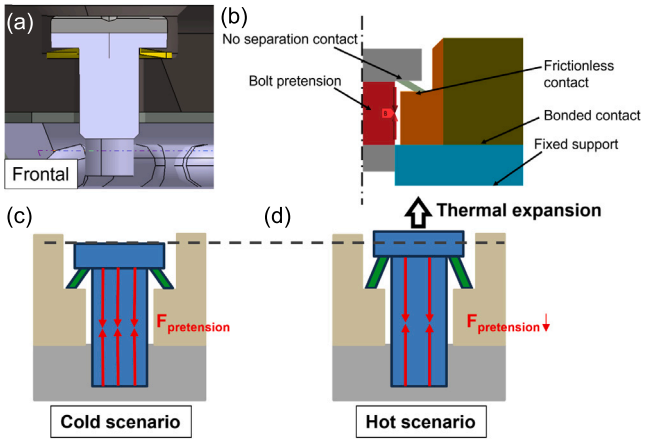

Fig. 8. (a) CAD view of the bolting between the front facing graphite tile and the stainless steel. Washers in yellow, the steel base of the bolt assembly in the lateral assembly is coloured in green.

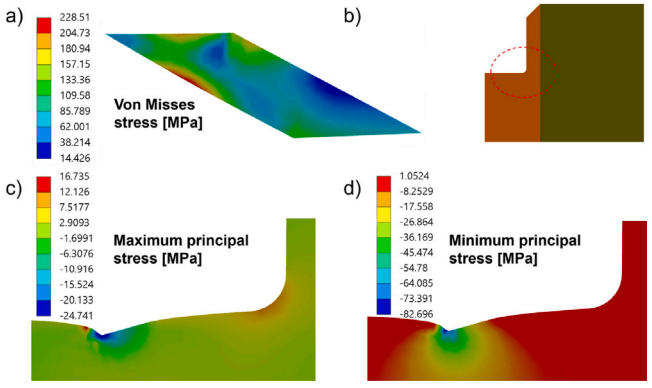

Fig. 9. (a) Von Mises stress in the inconel conical washer under the cold pretensioned conditions. (b) Diagram of the 2D Ansys model of the graphite tile cavity left for the bolt attachment. (c) Maximum and (d) minimum principal stress calculated in the graphite tile due to the pretensioned conical washer.

during any thermal expansion. Only a single washer could be used in the bolt assembly for the frontal graphite tile (as opposed to 2 washers in series for the lateral tiles) due to spatial restrictions. As the front tile is expected to experience the largest temperature increases an analysis of the stress due to the washer has been carried out in a dedicated model.

A 2D ANSYS model has been used to assess the impact of the pretension on the washer and on the graphite as the system is axisymmetric in geometry and in loads. A pretension of 600 N of the washers has been chosen based on similar graphite tiles attachments used across W7-X. Fig. 8b shows the model together with the pretension region and the chosen contacts and support. Both the cold pretensioned state illustrated in Fig. 8c and a hot, thermal expansion state has been analysed.

The results from this simulation are presented in Fig. 9. The washer withstands up to 230 MPa, while the yield limit on inconel is 550 MPa. For the graphite, the stress is concentrated in the inner corner where the tension and compression are low. It is important to note that the contact point between the washer and the graphite presents relatively high stresses, but this is most probably a numerical artefact and not a physical phenomenon. Nonetheless, a plain washer will be added in the assembly to distribute the load over a larger surface. To this end, the graphite hole has been deeper an extra 0.5 mm to add this plain washer. A detailed analysis of the hot scenario has found that the tensile and compressive stresses for this scenario are mild and do not represent any danger for the tile.

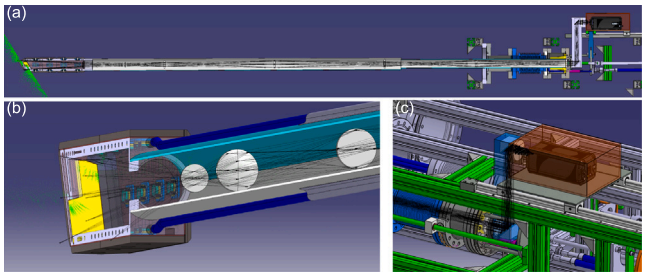

Fig. 10. (a) Side cross-sectional view of the sFILD indicating the layout of the optical elements and modelled rays. (b) CAD view of the scintillator to L3 lens including rays.

5. Optical relay system

The sFILD will make use of a system of optical lenses to image the scintillator plate onto an ex-vessel mounted CMOS camera (a C-Blue One 1608 × 1104 pix with 9 μm pix^{-1} from Firstlight). The camera will be mounted on a sliding sled which will be connected to the reciprocating manipulator arm so as to maintain a fixed optical path (of 3070 mm) to the scintillator plate at any insertion position of the diagnostic. Using Zemax a balance between simplicity (fewer lenses) and collecting brightness (more lenses) was struck during the design while a decision to use commercial off the shelf lenses as much as possible or with minimum modifications was adhered to.

A general layout of the optical elements is shown in Fig. 10a. The design makes use of 7 plano convex lenses, 6 mounted in-vessel in the manipulator arm and one mounted ex-vessel between two mirrors and a commercial objective lens to provide the final focal plane on the CMOS camera. Fig. 10b shows a view of the first three lenses. The system aperture is set by the first lens of 12 mm placed 500 mm after the scintillator plate. This results in F#41 system which corresponds to a numerical aperture (NA) of 0.012 and a collection angle of $\Omega = 4.7 \times 10^{-4}$ sr. The transmission coefficient of the system is calculated to be 3.1×10^{-4}. A non-symmetric distortion of the image is expected on two corners of the detector plate, due to the tilt of the scintillator plate w.r.t the optical axis. However this is relatively small under 1.5%. The system will have a 42 magnification ratio and spot size analysis indicates an imaging resolution of around 1 mm across the detector plate.

6. Synthetic FILD signal

In order to calculate the expected FILD optical signal from the CMOS camera, modelling was firstly carried out to determine the expected fast-ion losses onto the probe head as described in [4]. Here the full fast-ion orbit code ASCOT5 [12,13] was used. Fig. 11 illustrates the inclusion of the sFILD probe head in the ASCOT5 input wall geometry and shows two example loss orbits that impact onto the probe head. The sFILD probe head will have two entrance slits to measure both populations of lost fast ions in W7-X.

Fig. 12a shows a CAD of the probe head illustrating the orientation and positioning of the scintillator plate and the two entrance slits with example orbits entering the probe head. The head has been shaped such that the scintillator plate will be aligned with the magnetic field direction (parallel to the LCFS) in the standard magnetic field (referred to as the EIM) configuration. It should be noted that the variation in the magnetic field direction between the various field configurations

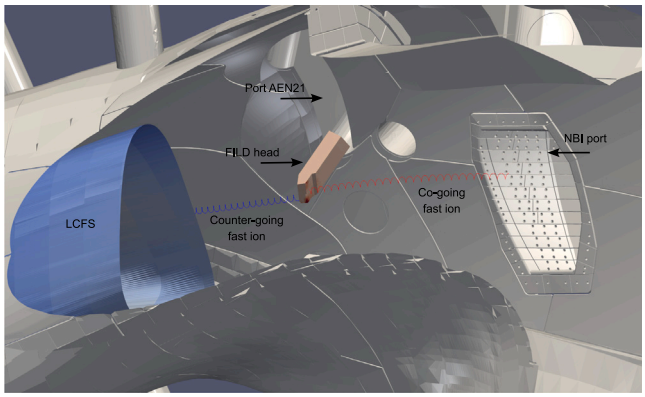

Fig. 11. Illustration of the model sFILD probe head included in the ASCOT5 input wall geometry. Two exemplary fast-ion orbits that collide with the detector as calculated by ASCOT5 are also shown.

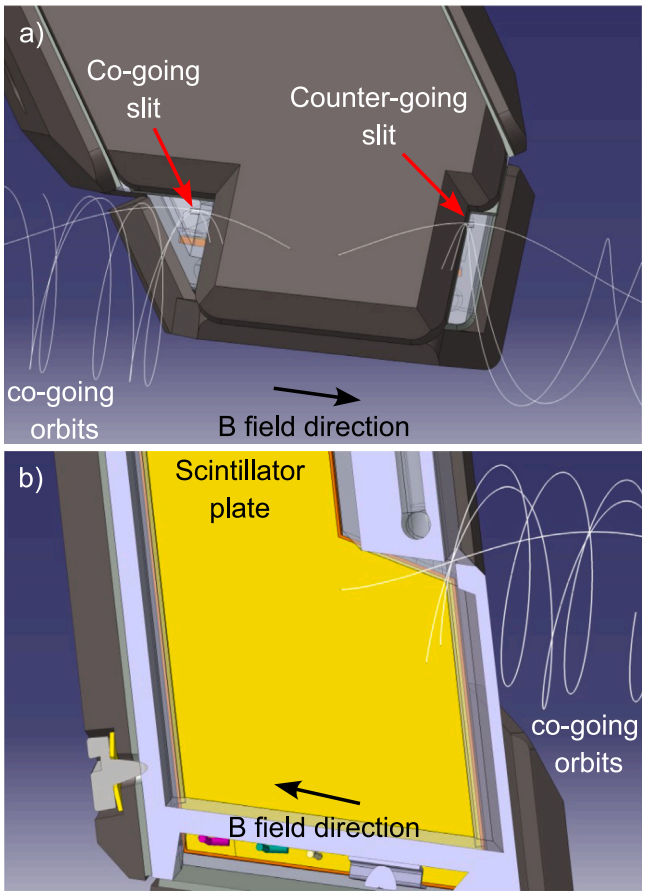

Fig. 12. (a) CAD view of the sFILD probe head illustrating position of the entrance slits along with example orbit trajectories entering the detector. (b) CAD cross-sectional view of the probe head as observed from the camera side with example co-going orbits impinging on the scintillator plate.

of W7-X is minimal at the probe head position. Due to the orientation of the AEN21 port, the scintillator plate is not perpendicular to the optical axis, however this has been considered in the optical design presented in the previous section. A great effort has been made to shape the probe head around the entrance slits to minimize self-shadowing of orbits and maximize the range of accepted pitch and energy. The FILDSIM code [14] has been used to determine the optimal position parameters of the entrance slits for optimal signal as well as for minimal self-shadowing of orbit trajectories. The optimal values for the slit sizes were found to be 1.5 mm by 0.9 mm, positioned 5 mm in perpendicular distance from the scintillator surface. The collimator heights were chosen to be 4 mm with the lengths 1.6 mm. Furthermore, FILDSIM was used to construct an instrument function based on the probe head CAD model to evaluate the expected synthetic signal.

Using the instrument function calculated from FILDSIM a synthetic signal is calculated given the theoretical loss distribution from ASCOT5 as well as the properties of the relay optics and camera sensor discussed in the previous section. Fig. 13 shows the expected camera signal corresponding to the loss distribution of fast-ion markers in the EIM configuration with the probe head at maximum insertion, corresponding to 7.5 cm from the LCFS. Two strike maps (corresponding to markers entering through the two slits) are plotted as red grids onto the synthetic camera frame. As can be seen both co- and counter-going losses are expected to be measured. Furthermore it is expected that the pitch distribution of the losses are well conserved, while a slight smearing out of the markers in the gyro-radius direction is observed.

7. Conclusion

The design and engineering analyses of a new scintillator based FILD for W7-X has been presented. Firstly, an assessment of the EM and structural loads on the sFILD has been performed. Analysing two possible cases of EM loads during disruption events found that only during a decay of the toroidal current is a torsional load (of 40 N m) expected on the probe head. A structural analysis of the sFILD, which takes into account possible EM loads, found that the expected deformation of the manipulator system under cantilever will be around 3.5 mm. This represents a 0.15% deformation w.r.t the length of the system under cantilever. The maximum expected stresses are observed to occur at the contact between the manipulator guiding support at the plasma facing end of the support structure and at a cut-out corner of the support structure itself. The magnitude of these stresses at both locations are around 48 MPa, well below the yield strength of the planned SS316LN stainless steel at 208 MPa.

Additionally, a vibrational analysis was performed both for vibrations from the electrical grid at 50 Hz and with uniform frequencies to conservatively estimate response to seismic vibrations or vibrations from unexpected sources. The deformations and stresses from the grid frequency is negligible, and for uniform vibrations with 1 g acceleration only small deformations (less than 4 mm) and stresses (less than 28 MPa) are calculated indicating no collision with the port structure should be expected.

Next, a series of analyses have been performed to determine the thermomechanical integrity of the graphite tiles and the bolting assembly of the sFILD diagnostic. The tiles have been shown to behave below material limits during parking and during measuring. The bolting assembly features a pretensioned bolt that will not damage the chosen washer. The contact between the conical washer and the graphite is not well resolved due to the complexity of said contact, nonetheless, no significant loads are expected there as the stress concentrator nearby presents low mechanical loads. As a safety measurement, some extra space has been allocated on the graphite to allow the addition of a plain washer that could spread the conical washer contact with the graphite if needed.

A design for the relay optics of the sFILD has also been presented. The design makes use of 7 plano-convex (off-the-shelf) lenses, two folding mirrors and a commercial objective lens attached to the camera allowing for final focusing. The optical system will have a F#41 equivalent to a NA of 0.012. Here, a balance between light gathering ability and the number of lenses and complexity was struck during the

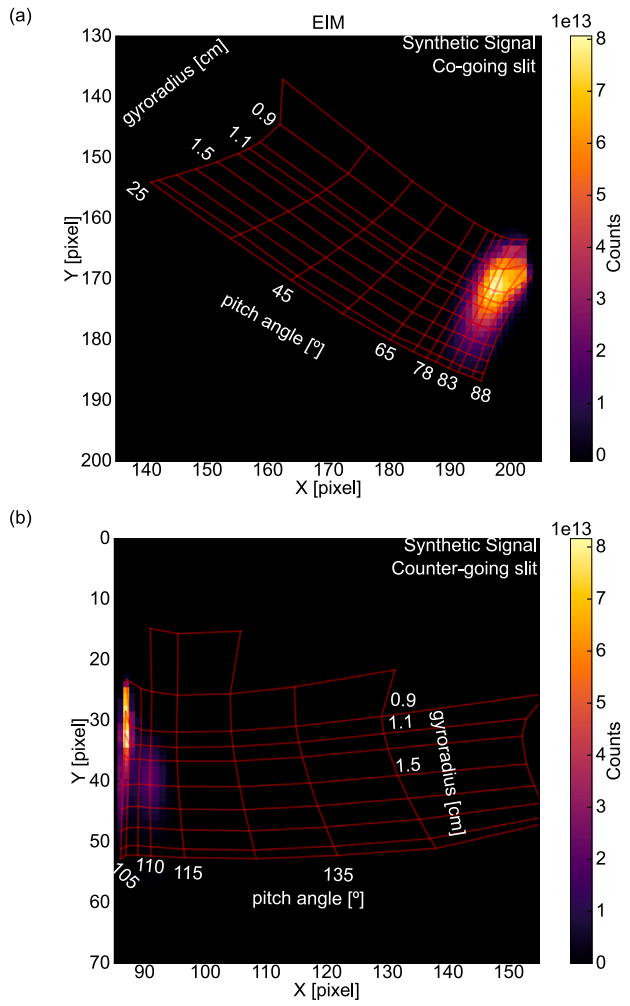

Fig. 13. Comparison of the synthetic (a) co-going and (b) counter-going camera signal for the standard magnetic field configuration.

design. The system is expected to have minimal imaging distortion (less than 1.5%) and a high optical resolution across the scintillator plate of around 1 mm.

Finally, a synthetic signal for the sFILD camera was calculated based on expected fast-ion losses calculated using the ASCOT5 code. Modelling shows both co- and counter-going losses can be expected. The instrument function of the designed probe head has been calculated using the FILDSIM code and used to forward model the expected camera signals. It was found that both populations of losses should be observable with a high pitch angle resolution, while a slight smearing out of the gyro radii can be expected in the measurements.

CRediT authorship contribution statement

A. Jansen van Vuuren: Writing – original draft, Visualization, Project administration, Methodology, Investigation, Formal analysis. **J. Garcia-Dominguez:** Visualization, Validation, Formal analysis. **J. Hidalgo-Salaverri:** Visualization, Validation, Formal analysis. **J. Segado-Fernandez:** Visualization, Validation, Formal analysis. **A. LeViness:** Project administration, Investigation, Formal analysis. **J. Ayllon-Guerola:** Validation, Supervision, Formal analysis. **J. Rueda-Rueda:** Visualization, Software. **S.A. Lazerson:** Validation, Resources. **J. Galdon-Quiroga:** Writing – review & editing. **M. Garcia-Munoz:** Supervision. **N. Pablant:** Writing – review & editing, Supervision, Project administration.

Declaration of competing interest

The authors declare that they have no known competing financial interests or personal relationships that could have appeared to influence the work reported in this paper.

Data availability

Data will be made available on request.

Acknowledgements

This work has been carried out within the framework of the EUROfusion Consortium, funded by the European Union via the Euratom Research and Training Programme (Grant Agreement No 101052200 — EUROfusion). Views and opinions expressed are however those of the author(s) only and do not necessarily reflect those of the European Union or the European Commission. Neither the European Union nor the European Commission can be held responsible for them.

References

[1] W. Lotz, P. Merkel, J. Nuhrenberg, E. Strumberger, Collisionless alpha - particle confinement in stellarators, Plasma Phys. Control. Fusion 34 (6) (1992) 1037–1052, http://dx.doi.org/10.1088/0741-3335/34/6/010.

[2] M. Drevlak, J. Geiger, P. Helander, Y. Turkin, Fast particle confinement with optimized coil currents in the W7-X stellarator, Nucl. Fusion 54 (7) (2014) 073002, http://dx.doi.org/10.1088/0029-5515/54/7/073002.

[3] E. Strumberger, Deposition patterns of fast ions on plasma facing components in W7-X, Nucl. Fusion 40 (10) (2000) 1697–1713, http://dx.doi.org/10.1088/0029-5515/40/10/302.

[4] A. Jansen van Vuuren, S.A. Lazerson, A. LeViness, M. Garcia-Munoz, D. Gates, J. Galdon-Quiroga, J. Hidalgo-Salaverri, J. Rueda-Rueda, J. Garcia-Dominguez, J. Ayllon-Guerola, Conceptual design of a scintillator-based fast-ion loss detector for the wendelstein 7-X stellarator, IEEE Trans. Plasma Sci. 50 (11) (2022) 4114–4119, http://dx.doi.org/10.1109/TPS.2022.3183890.

[5] K. Ogawa, S. Bozhenkov, S. Äkäslompolo, C. Killer, O. Grulke, D. Nicolai, G. Satheeswaran, M. Isobe, M. Osakabe, M. Yokoyama, R. Wolf, Energy-and-pitch-angle-resolved escaping beam ion measurements by faraday-cup-based fast-ion loss detector in Wendelstein 7-X, J. Instrum. 14 (09) (2019) C09021, http://dx.doi.org/10.1088/1748-0221/14/09/c09021.

[6] S.A. Lazerson, et al., Development of a Faraday cup fast ion loss detector for keV beam ions, Rev. Sci. Instrum. 90 (9) (2019) 093504, http://dx.doi.org/10.1063/1.5111714.

[7] M. García-Muñoz, H.-U. Fahrbach, H. Zohm, Scintillator based detector for fast-ion losses induced by magnetohydrodynamic instabilities in the ASDEX upgrade tokamak, Rev. Sci. Instrum. 80 (5) (2009) 053503, http://dx.doi.org/10.1063/1.3121543.

[8] P.J. Bonofiglo, V. Kiptily, A. Horton, P. Beaumont, R. Ellis, F.E. Cecil, M. Podesta, Improvements to the faraday cup fast ion loss detector and magnetohydrodynamic induced fast ion loss measurements in joint European Torus plasmas, Rev. Sci. Instrum. 91 (9) (2020) 093502, http://dx.doi.org/10.1063/5.0014278, arXiv:https://doi.org/10.1063/5.0014278.

[9] S. Marsen, Y. Corre, H. Laqua, V. Moncada, D. Moseev, H. Niemann, M. Preynas, T. Stange, T.W.-X. Team, First results from protective ECRH diagnostics for Wendelstein 7-X, Nucl. Fusion 57 (8) (2017) 086014, http://dx.doi.org/10.1088/1741-4326/aa6ab2.

[10] J. Fellinger, U. Lippmann, H. Greve, M. Alhashimi, M. Schülke, S. Äkaslompolo, P. Drewelow, M. Jakubowski, R. König, A. Lorenz, Design of endoscopes for monitoring water-cooled divertor in W7-X, Fusion Eng. Des. 158 (2020) 111841, http://dx.doi.org/10.1016/j.fusengdes.2020.111841, [Online]. Available:https://www.sciencedirect.com/science/article/pii/S0920379620303896.

[11] J. Hidalgo-Salaverri, J. Gonzalez-Martin, J. Ayllon-Guerola, M. Garcia-Munoz, B. Sieglin, J. Galdon-Quiroga, D. Silvagni, E. Viezzer, J. Rueda-Rueda, T. Lunt, A. Herrmann, the ASDEX Upgrade team, Thermo-mechanical limits of a magnetically driven fast-ion loss detector in the ASDEX Upgrade tokamak, J. Instrum. 17 (02) (2022) C02020, http://dx.doi.org/10.1088/1748-0221/17/02/C02020.

[12] E. Hirvijoki, et al., ASCOT: Solving the kinetic equation of minority particle species in tokamak plasmas, Comput. Phys. Comm. 185 (4) (2014) 1310–1321, http://dx.doi.org/10.1016/j.cpc.2014.01.014.

[13] J. Varje, et al., High-performance orbit-following code ASCOT5 for Monte Carlo simulations in fusion plasmas, arXiv (2019) arXiv:1908.02482.

[14] J. Galdon-Quiroga, et al., Velocity-space sensitivity and tomography of scintillator-based fast-ion loss detectors, Plasma Phys. Control. Fusion 60 (10) (2018) 105005, http://dx.doi.org/10.1088/1361-6587/aad76e.